Synthesis of a Lattice-Resolved Laminate-Structured Perovskite Heterointerface

Zhimin Li[1,3], Pengfei Guo[2,3], Yalan Zhang[2], Weizhen Wang[1], Songhua Cai[1,*], Yuanyuan Zhou[2,*]

[1] Department of Applied Physics, The Hong Kong Polytechnic University, Kowloon, Hong Kong SAR, China

[2] Department of Chemical and Biological Engineering, The University of Science and Technology, Clear Water Bay, Hong Kong SAR, China

[3] These authors have contributed equally.

*Correspondence should be addressed to: songhua.cai@polyu.edu.hk ; yyzhou@ust.hk

Abstract

2D surface passivation has been shown to be useful for achieving state-of-the-art perovskite optoelectronics, and the microstructural and phase heterogeneities of 2D perovskite passivators can influence their roles. However, the synthesis of co-homogenized, stable microstructure and phase in such passivators remains challenging. Herein, we leverage a [6,6]-phenyl-C61-butyric acid methyl ester (PCBM) molecular interlayer to mediate the reaction of 2D passivator and perovskite, leading to a uniform phase-purer 2D perovskite capping layer. This PCBM interlayer further mitigates grain-boundary etching encountered in conventional approaches, creating molecular passivation directly onto the perovskite surface. The inverted PSCs made as such feature a laminate-structured perovskite heterointerface at the electron-extracting side, which contributes to improved charge energetics and film stability, owing to regulated band transition and laminate-layer protection, respectively. Power conversion efficiencies up to 26% are achieved, together with enhanced device stabilities under ISOS-standardized protocols, showing T_{90} lifetimes over 1,000 h in both the damp-heat test (85 °C, 85% relative humidity) and maximum-power-point tracking under one-sun illumination. Lattice-resolved insights are provided to link the microstructure to device performance, shedding light on the significance of passivator-microstructure uniformity and reliability on the performance of perovskite optoelectronics.

Introduction

Perovskite solar cells (PSCs) have emerged as a future photovoltaic (PV) technology due to their potential for combining low cost and minimal carbon footprint in industrial manufacturing.[1-3] According to the sequence of depositing the device layers, PSCs are categorized into two types: regular (*n*-*i*-*p*) and inverted (*p*-*i*-*n*) PSCs. While advancements have been made in both types, regular PSCs have faced greater challenges regarding stability in real-world applications, primarily to the use of the lithium-doped Spiro-OMeTAD as the hole-transporting layer (HTL).[4,5] Consequently, inverted PSCs have garnered substantial attention in recent years and have achieved the highest power conversion efficiencies (PCEs).[6,7] In state-of-the-art inverted PSCs, self-assembled monolayers are used as the HTLs on the *p* side, creating intimate interfacial contacts and passivation, which result in superior PCEs and stability compared to regular PSCs. However, in inverted devices, the perovskite heterointerface on the *n* side remains relatively less ideal because of the limited molecular interaction of the fullerene-based electron-transporting layer (ETL) with the perovskite top surface.[8-10] In this regard, 2D perovskites or their related organic molecules have been incorporated as a type of effective top-surface passivators that can not only reduce the non-radiative recombination centers but also serve as a structurally capping layer to protect the film from environmental influences such as moisture ingress.[11-14] Numerous efforts have been made to tailor the molecular structures of 2D perovskite passivators with various organic cations, which have proven useful in achieving improved PCEs and stabilities in PSCs.[15-19] However, to date, detailed investigations into the heterointerface microstructures of 2D perovskite passivators remain rare, which may unlock new opportunities bringing up the level of device performance as well as contributing to revealing the passivation mechanisms.

In this work, by leveraging the lattice-resolved analysis capability of scanning transmission electron microscopy (STEM), we observed nontrivial microstructural and phase heterogeneities in the 2D surface passivation layer deposited using the conventional method. This layer featured a discontinuous capping-layer microstructure and a random mixture of 2D perovskite phases with different octahedral-layer numbers (n = 2-5). We attributed this phenomenon to the uncontrolled interfacial reaction of the used 2D molecular salts with the 3D perovskite top surface, which also resulted in a detrimental morphological etching of grain boundaries due to their relatively high chemical reactivity. To mitigate these microstructural demerits, we demonstrated an unconventional route of surface passivation in which the reaction of 2D molecular salts with the 3D perovskite top surface is mediated via a “molecular sieve” layer of [6,6]-phenyl-C61-butyric acid methyl ester (PCBM). This route creates a laminate-structured surface (LSS) successively stacked by a 2D molecular layer, a PCBM interlayer, and a 2D perovskite layer of only n = 1 and 2 phases. The resultant LSS-based inverted PSCs achieved PCEs of up to 26%, together with highly improved damp-heat and operational stabilities. Importantly, based on further STEM studies, we found that the LSS microstructure and phase have been well retained in the aged PSCs even after long-

term stability tests, which can be attributed to the ion-blocking effects of the PCBM interlayer. This contrasts with the substantial microstructure and phase changes seen in control devices. This work highlights the importance of synthesizing uniform, stable passivator microstructures for perovskite photovoltaics and beyond.

Synthesis and lattice-resolved STEM analysis

For synthesizing the LSS sample, we first spin-coated an ultrathin interlayer of PCBM molecules (5 mg/mL solution in chlorobenzene (CB)) onto the surface of 3D $FA_{0.9}Cs_{0.1}PbI_3$ perovskite thin film and then spin-coated a 2D molecular salt - phenethyl ammonium iodide (PEAI) based solution in isopropanol (IPA; 10 mg/mL), followed by mild thermal annealing at 100 ºC. As schematically illustrated in **Fig. 1a**, the sandwiched, ultrathin PCBM interlayer serves as an inert "molecular sieve", allowing controlled ion penetration and exchange between the 3D perovskite and top surface sides. The PCBM-mediated interfacial reaction exhibits a much-reduced rate and enables the formation of a uniform LSS microstructure. We also prepared a control PEAI-treated film sample without the involvement of the PCBM interlayer. We first compared the surface morphologies of the LSS and control samples using scanning electron microscopy (SEM). As seen in **Supplementary Fig. 1**, when a PCBM interlayer is applied, the perovskite film after PEAI deposition exhibits a uniform contrast in SEM, indicating a uniform 2D perovskite coverage that preserves the original 3D perovskite topography (**Supplementary Fig. 1a, b**). In contrast, the control sample exhibits an irregular distribution of 2D perovskite phases (**Supplementary Fig. 1c, d**).

To gain an in-depth understanding of the perovskite heterointerface, we employed low-dose scanning transmission electron microscopy (STEM) to study the film's cross-sectional microstructures. The capability of cross-sectional STEM observations to acquire lattice-resolved interface microstructural information has been demonstrated by several research works.[11,12,20-24] **Fig. 1b-c** show the lower-magnification STEM images of both LSS and control films acquired in high-angle annular dark field (HAADF) mode. **Fig. 1b** reveals that the LSS sample maintains an intact surface of 3D perovskite grains compared with the control sample under the same PEAI treatment condition. The PCBM interlayer (the dark contrast sandwiched layer) has a characteristic thickness of ~10 nm measured from the HAADF-STEM image, on top of which is a continuous, uniform layer of 2D perovskite (~10 nm, typically 5-15 nm thick). In contrast, as seen in **Fig. 1c**, in the control film, the 3D perovskite grains do not maintain their original surface microstructure after the PEAI treatment. A discontinuous layer consisting of randomly distributed 2D perovskite crystals is formed on top of the 3D perovskite grains. The thickness of this layer can vary widely from 15 to 50 nm, and there is partial deterioration of the original 3D perovskite grain surfaces (**Fig. 1c**). This surface irregularity is attributed to the uneven and vigorous cation-exchange reaction between the 3D perovskite surface and the 2D organic spacer cation PEA^+. Notably, an increase in the PEAI concentration leads to a rise in the thickness and coverage of the 2D

perovskite, and the surface deterioration becomes more evident when the PEAI concentration is increased to 15 mg/mL (**Supplementary Figs. 2**, **3**). Even when the PEAI is diluted to 3 or 5 mg/mL, the formation of 2D perovskite will lead to evident erosion to the 3D grain surface (**Supplementary Fig. 4**). However, in the LSS sample, the ultrathin PCBM interlayer is formed with closely packed sphere-shaped molecules, inherently containing nanochannels that allow a steady interlayer transport of PEA^+, $FA^+/Cs^+/I^-$ and Pb^{2+} upon thermal annealing. This slows down the reaction process. What is also important is that the chemically inert PCBM interlayer geometrically constrains the growth of as-formed 2D perovskite and molecular passivation layers. These factors contribute to the lateral homogeneity of the reaction front, which is essential to the control over the interfacial morphologies and the minimized impact on the 3D perovskite grain surface microstructure (**Supplementary Fig. 5**).

To confirm the ion exchange through the ultrathin PCBM interlayer, we prepared another LSS sample by applying the same PCBM and PEAI treatments to a 3D $FA_{0.9}Cs_{0.1}PbBr_3$ perovskite film to track the transport of interfacial halide anions. Using a bromide instead of an iodide sample facilitates the differentiation of halide anions supplied by the PEAI or the surface region of 3D perovskite grains during this reaction process. Using the STEM electron energy loss spectroscopy (EELS) analysis, we observed the co-existence of I^- and Br^- on the 3D grain surface and the 2D capping layer, confirming the bi-directional ion exchange between the PEAI salt and 3D grain surface through the PCBM molecular sieve (**Supplementary Fig. 6**). To examine the distribution of the PEA^+ within the LSS structure, the energy-loss near-edge structures (ELNES) of nitrogen (N) K-edge was analyzed (**Fig. 1j-l**). Within the 2D perovskite layer and the PCBM interlayer (regions I-IV in **Fig. 1k**), the N K-edge structure features a main peak at 408.5 eV and a small pre-peak at 400.5 eV, consistent with the dominant C-N σ bond characteristics (π bond at around 400 eV, σ bond at around 408 eV) and confirms the presence of PEA^+ (**Fig. 1j**).[25] Additionally, the increased N K-edge signal intensity beneath the PCBM interlayer (region IV in **Fig. 1j**) indicates a concentration of PEA^+ on the surface of the 3D grains. This concentration of PEA^+ on the 3D grain surface is evident in various LSS regions (**Supplementary Fig. 7**). As a result, 2D monolayers can be found in certain regions of the 3D grain surface (**Supplementary Fig. 8**), suggesting that the residual PEA^+ tends to form a 2D molecular passivator covering the 3D grains. Based on this mechanism, we found that the thickness of the PCBM interlayer affects the microstructure and phase of the 2D perovskite capping layer. We prepared PCBM interlayers with varying thicknesses from 0 to 60 nm by spin-coating a PCBM solution with 1, 2, 3, 5, and 10 mg/mL concentrations. The 2D perovskite capping layer tends to be smoother and more continuous with an increase in the PCBM thickness, as shown in **Supplementary Fig. 9**. However, once the concentration of PCBM reaches 10 mg/mL, the interlayer can become as thick as 60 nm. The thick PCBM interlayer causes difficulties with ion exchange, inhibits the 2D layer from remaining continuous, and drastically reduces its thickness. The dependence of the PCBM interlayer thickness for the interfacial reaction kinetics is consistent with our earlier proposed PCBM-mediation mechanisms.

The *n*-value distribution and orientation of 2D perovskites, which are important for managing band gaps and transporting carriers, are subjects that require further research. For the control samples without interlayer, as the magnified HAADF-STEM image of the chosen area in **Fig. 1c**, **Fig. 1g** shows multiple layers of 2D perovskite with varying thickness formed on top of the visibly rough 3D grain surface. **Fig. 1h** is an enlarged image with the direction and region indicated by the arrow in **Fig. 1g**, and **Fig. 1i** shows the signal intensity line profile of **Fig. 1h**. The 2D perovskite structure in **Fig. 1h** is well-correlated with the layer distance measured in **Fig. 1i**. The line profile study reveals that, in the control sample, the *n*-value arrangement of 2D perovskites is disorderly, with $n = 2$ (interlayer spacing $d = 2.20$ nm) being the primary component, as well as 2D perovskites with $n = 3$ (interlayer spacing $d = 2.94$ nm) and $n = 5$ (interlayer spacing $d = 4.18$ nm). Additionally, we noticed that control samples have 2D perovskite with varied orientations while having the same *n* value on flat 3D grain surfaces (**Supplementary Fig. 10**), whereas 2D perovskites with a high *n* value doped with a low *n* value are commonly found at undulating grain boundaries (**Supplementary Figs. 11, 12**). This can be attributed to the rapid formation of 2D perovskite during the contact between the PEAI solution and the 3D grain surface. The interaction between PEA^+ and the remaining PbI_2 (**Supplementary Fig. 13**), as well as the considerable amount of free $FA^+/Cs^+/I^-$ (**Supplementary Fig. 14**) on the 3D grain surface, increases the possibility that some 2D perovskite with an uneven *n* value may not develop in a surface-parallel orientation and may cause more damage to 3D grains (**Supplementary Fig. 15**). When it comes to the LSS sample, a magnified image of the region in **Fig. 1b** is shown in **Fig. 1d**. Spin-coating the PEAI solution on the interlayer instead of directly on the 3D grains results in an ultra-thin 2D perovskite layer, such as the two octahedral layers of $n = 2$ 2D perovskite seen in **Fig. 1e** and **Fig. 1f**, which are enlarged images of the arrowed region in **Fig. 1d** and its corresponding intensity line profile. Due to the protective effect of PCBM, PEA^+ struggles to bind enough A-site ions and $[PbI_4]^{2-}$ in LSS samples, making it difficult for 2D perovskites with $n > 2$ to crystallize. Furthermore, generating high *n*-value 2D perovskite becomes increasingly challenging as the distance from the 3D grain surface increases. This allows 2D perovskite in LSS to be arranged $n = 2$ to $n = 1$ (**Supplementary Fig. 16**), which can enhance carrier transport efficiency in *p-i-n* devices.[12,14] Additionally, the fraction of PbI_2 in 3D perovskite may also influence the *n* phases of 2D perovskite in the LSS sample. As shown in **Supplementary Fig. 17**, a deficiency of PbI_2 may hinder the formation of the $n = 1$ phase 2D perovskite, whereas the proportion of the $n = 1$ phase tends to increase with excess PbI_2 (**Supplementary Fig. 17a, b**). STEM observations also show more $n = 1$ phase 2D perovskite in the LSS sample prepared with $(FAI)_{0.9}(CsI)_{0.1}(PbI_2)_{1.15}$ 3D perovskite (**Supplementary Fig. 17f**).

4D STEM of near-surface grain boundaries

The interaction between the PEAI salt and 3D perovskite may also influence the integrity of near-surface grain boundaries, critical to the performance of resultant PSC devices. [6,26-31] As conventional STEM imaging falls short of revealing the underlying crystalline structure, we employed a combination of four-dimensional STEM (4D-

STEM)[32,33] and nano-beam electron diffraction (NBED) techniques[34-37] to probe the microstructure and lattice orientation distributions in both the control and LSS samples. In the control film without the ultrathin PCBM interlayer, HAADF-STEM identifies a dark-contrast region beneath the 3D grain surface (**Fig. 2a**), which is determined as n = 2 2D perovskite by the corresponding NBED pattern (region i of **Fig. 2a**), nearly perpendicular to the 2D perovskite above the 3D grain (region ii of **Fig. 2a**). The NBED patterns of the 3D grains (regions iii and iv of **Fig. 2a**) demonstrate a typical orthogonal structure (space group *Pbnm*, a = 0.8646 nm, b = 0.8818 nm, c = 1.2520 nm), with the left and right segments exhibiting different orientations. To accurately represent the deformation of 3D grains, a virtual bright-field (BF) STEM image was reconstructed from the 4D diffraction dataset, as presented in **Fig. 2b** and **Supplementary Fig. 18**. This image clearly shows that the grain boundary and adjacent regions of the 3D grains are eroded by the 2D perovskite growing parallel to the grain boundary. In contrast, when it comes to the LSS sample, the HAADF-STEM image displays a distinct separation between the 3D grains and 2D perovskite by a thin PCBM interlayer (**Fig. 2c**). The NBED pattern of the 2D perovskite, as depicted in NBED **Fig. 2c** (region i), indicates that the orientation of the 2D perovskite layer is approximately parallel to the surface of the 3D grains. Within this context, three distinct 3D perovskite grains, each with a unique orientation, are discernible from the 4D diffraction dataset (NBED of regions ii-iv in **Fig. 2c** and **Supplementary Fig. 19**). The reconstructed BF-STEM image (**Fig. 2d**) confirms that the surfaces and grain boundaries of the 3D grains are well-preserved, with no evidence of grain boundary etching by the 2D perovskite, underscoring the protective role of the PCBM interlayer.

Optoelectronic properties and chemical stability

We performed X-ray diffraction (XRD) on the LSS and control films (**Fig. 3a**). In both cases, the passivation does not notably change the crystallinity and grain orientation of the pristine 3D perovskite films (**Supplementary Fig. 20**). Nevertheless, the use of the PCBM interlayer influences the overall phase distribution and orientation of as-formed 2D perovskite capping layer. Moreover, we did not observe any notable change in the bandgap (E_g) of the underlying 3D perovskite according to the normalized photoluminescence (PL) spectra (**Fig. 3b**), further attesting to the preservation of bulk 3D perovskite phase in both LSS and control films. Interestingly, the PL spectrum of the LSS sample shows dominant emission peaks corresponding to n = 1 and 2, whereas PL emissions associated with $n \geq 3$ phases become more pronounced in the control sample (**Fig. 3b**), in accordance with the STEM observation. In **Supplementary Note 1**, we elaborated on additional observations on the XRD and PL results in **Fig. 3**. More importantly, the 2D perovskite (n = 1 and 2) capping layer formed uniformly on top of 3D perovskite surfaces in the LSS samples, as shown in the PL images in **Fig. 3c**, indicating that the PCBM interlayer can induce uniform growth and distribution of 2D perovskites. We further monitored the PL emission centered at the 3D peak (~780 nm). We observed a uniform emission over a large area of 15 μm by 15 μm from the underlying 3D perovskite layer, confirming uniform 2D passivation for 3D perovskite

films with the PCBM interlayer. Then, we employed steady-state and time-resolved PL spectra to investigate the effects of the PCBM interlayer on carrier dynamics at the perovskite heterointerface (**Fig. 3d-g**). The detailed fitting parameters of our PL results are summarized in **Supplementary Table 1**. The LSS and control samples were deposited on glass substrates. When the laser is incident from the glass side (bottom direction), the control sample exhibits stronger PL emission with a longer decay lifetime than pristine 3D perovskite films because of the suppression of nonradiative recombination associated with trap states at the surface (**Fig. 3d**). After incorporating the PCBM interlayer, the LSS sample shows much stronger PL emission and further increases the average PL lifetime from 427 ns (control sample) to 925 ns (**Fig. 3f**), indicating that the unique laminate structure can further enhance the optoelectronic quality of 3D perovskite films. Interestingly, when the laser is incident from the perovskite side (top direction), a more effective PL quenching occurs in the LSS films compared to pristine 3D and control samples (**Fig. 3e** and **Fig. 3g**). Such quenching is due to charge extraction at the 3D-2D interface, suggesting that the PCBM interlayer could help achieve better charge separation. The average carrier lifetime of LSS films is nearly threefold shorter than control films.

Subsequently, the stability of LSS and control films was explored in relative humidity (RH) of 75±10%. To quantify the film degradation, we recorded the normalized absorbance decay of the 2D peak at ~560 nm corresponding to $n = 2$ and the bandgap evolution of the 3D perovskite for both the control and LSS samples during the aging test (**Supplementary Fig. 21**).[14] As shown in **Fig. 3h**, the control films exhibited gradual decreases in the intensity of the 2D peak and the bandgap of the 3D perovskite after 55 days. In contrast, the LSS films retained their integrity, with no degradation of their 2D and 3D structures, demonstrating outstanding chemical stability with improved resistance to moisture ingression.

Photovoltaic performance and device stability

We evaluated the effects of laminate-structured perovskite heterointerface on the photovoltaic performance of inverted PSCs with the configuration of ITO/MeO-2PACz/perovskite/PCBM/BCP/Ag (**Fig. 4a**), where the perovskite film with the composition of $Cs_{0.05}(MA_{0.05}FA_{0.95})_{0.95}Pb(I_{0.95}Br_{0.05})_3$ was used as the active layer of PSCs (donated as CsFAMA, 1.57 eV bandgap, **Supplementary Fig. 22**). The effects of the concentrations of the PCBM and PEAI on photovoltaic performance were systematically studied. The optimal concentration for both PEAI and PCBM was 5 mg/mL (**Supplementary Fig. 23**, **Table 2**, **Table 3**, and **Note 2**). As shown in current density-voltage (*J-V*) curves in **Fig. 4b**, the champion control devices exhibited a decent PCE of 24.42% under reverse scanning, higher than that of pristine 3D devices (without 2D surface treatment, 20.30%) owing to the general passivation effect of 2D perovskite, whereas the champion efficiency of the LSS-based devices is further increased up to 25.97%, ascribed to the enhancement of all photovoltaic parameters with open-circuit voltage (V_{OC}) from 1.179 V to 1.206 V, short-circuit current density (J_{SC}) from

24.57 mA/cm^2 to 25.02 mA/cm^2, and fill factor (FF) from 84.31% to 86.08%. More importantly, the LSS devices exhibited negligible hysteresis (hysteresis index (HI), 0.81%) when measured in both reverse and forward scanning (**Supplementary Table 4**), which is smaller than that of the pristine 3D (6.75%) and control (3.40%) devices. Further hysteresis analyses of *J-V* curves for different PSCs are provided in **Supplementary Fig. 24** and summarized in **Supplementary Note 3**. Additionally, the resultant LSS-based devices exhibit better reproducibility compared with those of the 3D and control devices, as indicated by the statistics of 50 individual devices under each condition in **Supplementary Fig. 25**. The average PCEs rise increasingly from 17.27% for 3D to 22.98% for control, and to 24.69% for LSS, attributed to enhancements in all photovoltaic parameters.

We further determined the E_g of the LSS device by differentiating its external quantum efficiency (EQE) spectrum, which exhibits an inflection point at 792 nm, corresponding to 1.57 eV (**Supplementary Fig. 26**).[38] Therefore, the V_{OC} deficit (E_g -qV_{OC}) of the LSS device was calculated to be 0.364 V,[39] which is among the lowest values reported so far for PSCs with an E_g of ~1.57 eV (**Supplementary Fig. 27**). Additionally, the integrated J_{SC} from the EQE matched well with the value extracted from the *J-V* curve (**Supplementary Fig. 26**). The enhanced EQE in the long wavelength range of 650 to 780 nm is mainly attributed to the optimized energy-level arrangement at the interface between the perovskite film and the PCBM ETL. To assess the interfacial energy-level alignments, we conducted ultraviolet photoelectron spectroscopy (UPS) tests for different perovskite films (**Supplementary Fig. 28** and **Note 4**). **Fig. 4c** shows the energy-level diagrams of MeO-2PACz anchored on the ITO substrate, perovskites, and PCBM. We observed that the secondary electron cut-off ($E_{cut\text{-}off}$) shifted to a higher binding energy after PEAI post-treatment regardless of the PCBM interlayer, indicating that the ion exchange-induced 3D to 2D perovskite phase transition could lower the Fermi level (E_F) of the perovskite films. Notably, the energetic gap between E_F and the valence band maximum (VBM) of the LSS film was wider than that of the control, indicating the enhanced *n*-type character of 3D perovskite films.[14] Additionally, the conduction band minimum (CBM) of LSS films was closer to the CBM of PCBM at the *n*-type contact, which resulted in more efficient charge transfer at the interface between the perovskite and the PCBM ETL. In contrast, the CBM of control films was much higher than the CBM of PCBM ETL with less *n*-type character, resulting in less efficient charge transfer of this at the electron-selective contact. Such an energy-level arrangement of LSS-based PSCs is conducive to the increase in the build-in electric field of their PSC devices and results in less charge accumulation at the electron-selective contact interface, thus contributing to the high V_{OC} and FF of PSCs, as evidenced by the Mott-Schottky (M-S) analyses (**Supplementary Fig. 29**).

We then conducted a series of durability tests for different PSC devices under various external stressors. We initially monitored the PCE evolution under continuous one-sun illumination in a nitrogen atmosphere (**Supplementary Fig. 30**). The photo-stability of LSS-based devices is superior to that of the control devices, maintaining 90%

(T_{90}) of their original PCE after 1,000 hours of illumination, while the control devices retained only 22% of their initial PCE after 768 hours. The remarkable enhancement observed is attributed to the blocking of ionic exchanges between 3D and 2D perovskites in the presence of the PCBM interlayer, evidenced by the electronic analysis (**Supplementary Fig. 31 and Note 5**). We then performed maximum power point (MPP) tracking tests under continuous light (100 mW cm^{-2}) following the ISOS-L-1l protocol. Typically, after 1,100 h, the LSS-based device still maintained 95% (T_{95}) of its initial PCE (**Fig. 4d**), whereas, for the control device, the PCE dropped to 40% of its initial value after only 450 h. Furthermore, we placed encapsulated devices in a chamber for the damp heat test (85°C and 85% RH) following the International Summit on Organic Photovoltaic Stability (ISOS) ISOS-D-3 protocol.[29] As shown in **Fig. 4e**, the LSS devices maintained 90.7% of their initial PCEs (23.02 ± 0.53%, **Supplementary Fig. 32**) over 1,000 hours under damp heat aging. In contrast, the control devices retained only 24.6% of their initial PCEs (21.08 ± 1.19%) within 500 hours. It is worth noting that the well-retained heterointerface microstructure after aging contributes to the better damp-heat durability of the LSS film, while for the control film without the PCBM interlayer, both the 2D and 3D components fail to maintain structural integrity, especially at the grain boundary region (**Fig. 4f-g**). To gain a more mechanistic understanding, we compared the degradation behaviors of the LSS and control devices in the maximum power point (MPP) operational and ambient conditions. As illustrated in **Supplementary Fig. 33**, the 3D and 2D perovskite layers are seen in both the fresh control and LSS devices. After 15 days of the MPP operation, the control device shows substantial microstructural degradation and the formation of PbI_2, particularly at the grain boundaries (**Supplementary Fig. 34a, b**). Conversely, the LSS device exhibits only minor damage, primarily at the buried interface, while the LSS structure remains mostly intact (**Supplementary Fig. 34c, d**). Thus, it is deduced that the degradation in the control device in MPP conditions is primarily attributed to the ion migration, which is known preferably along grain boundaries, triggering the observed microstructural change and phase degradation. In the LSS devices, ion migration is effectively blocked by the unique combination of the uniform 2D layer, the PCBM interlayer, and the 2D molecular layer. The degradation behaviors of the control and LSS samples in the ambient conditions are also very different. After being stored in a 50-60% relative humidity (RH) atmosphere for 10 days, the control sample's surface morphology changes dramatically, with the emergence of numerous pinholes (**Supplementary Fig. 35a, b**). In contrast, the LSS sample shows minimal surface changes (**Supplementary Fig. 35c, d**). STEM observations reveal that a large amount of PbI_2 forms in the 3D grains of the control sample (**Supplementary Fig. 36a, b**). Meanwhile, the LSS sample experiences little change with almost no PbI_2 formation (**Supplementary Fig. 36c, d**). We attribute the stability improvement under operational and ambient conditions mainly to the ion and moisture blocking effects of the PCBM interlayer and passivators within the LSS structure, in which the well-retained LSS microstructure and phase within the PSC devices reinforces the interface reliability and chemical stability of 3D perovskites.

Conclusions and outlook

This work demonstrates the use of a PCBM molecular interlayer in synthesizing a laminate-structured surface (LSS) for stabilizing PSCs. By mediating the reaction between 2D perovskite passivators and the underlying 3D perovskite layer, the PCBM interlayer promotes the formation of a uniform phase-purer 2D perovskite capping layer and a molecular passivation layer on the 3D perovskite surface. Detrimental grain boundary etching, generally encountered in the conventional passivation approach, is also alleviated. The unprecedented LSS benefits interfacial carrier transport and stability, leading to highly efficient and stable inverted PSCs. This study leverages cross-sectional high-resolution low-dose STEM methodology to investigate the interfacial morphology of the 2D passivation microstructure and 4D-STEM NBED analysis to determine the structural integrity of grain boundaries in 3D perovskite layer. These lattice-resolved analyses underscore the critical role of fundamental surface microstructures in optimizing device performance and stability. The PCBM molecular interlayer approach can be expanded to form LSS types with various tailored characteristics by adopting other passivation-mediating molecules, creating a new path for advancing perovskite solar cell and module technologies.

Methods

Chemicals and materials. Lead iodide and lead bromide (PbI_2 and $PbBr_2$, >99.99%) were acquired from TCI (Japan). Formamidinium iodide and methylammonium chloride (FAI and MACl, >99.99%) were purchased from Great-cell Solar (Australia). 4-tert-butylpyridine (4-TBP, 96%), bis(trifluoromethane) sulfonimide lithium salt (Li-TFSI, 99.95%), N, N-dimethylaniline (DMF) and dimethyl sulfoxide (DMSO), acetonitrile (ACN), chlorobenzene (CB), ethyl acetate (EA), isopropyl alcohol (IPA) were purchased from Merck (USA). Phenyl-C61-butyric acid methyl ester ($PC_{61}BM$), C_{60}, bathocuproine (BCP), and phenethyl ammonium iodide (PEAI), phenethyl ammonium bromine (PEABr) were purchased from Xi'an Polymer Light Technology Corp. Tin (IV) oxide (15 wt.% in H_2O colloidal dispersion) and cesium iodide (CsI, >99.998%) were acquired from Alfa Aesar (USA). Spiro-OMeTAD (99.8%) was purchased from Borun Chemical Co., Ltd. (China). MeO-2PACz was acquired from the Tokyo Chemical Industry. All materials were utilized without further purification.

Preparation of thin film samples. The ITO substrates underwent a cleaning process involving ultrasonic treatment with deionized water, acetone, and isopropanol for 20 minutes each, followed by UV ozonation. The tin (IV) oxide colloidal was diluted with deionized water at a volume ratio 1:5, followed by filtration and uniform spin-coating at 3000 rpm for 30 seconds. Subsequently, the sample was annealed at 180 ℃ for 30 minutes. For the fabrication of $FA_{0.9}Cs_{0.1}PbI_3$ perovskite films, a 1.4 M precursor solution was prepared by dissolving PbI_2 (645.4 mg), FAI (216.7 mg), CsI (36.4 mg), and MACl (28.3 mg) in 1 mL of a DMF/DMSO solvent mixture (4:1 volume ratio). The mixture was stirred overnight at room temperature and filtered through a 0.22 μm syringe filter before use. The perovskite film was formed via a consecutive two-step spin-coating process at 1,000 rpm. for 10 s and 4,000 rpm. for 30 s. During the second step, 200 μL EA was poured onto the substrate 20 s before program completion. The substrate was then annealed on a hotplate at 160 °C for 10 minutes, forming the $FA_{0.9}Cs_{0.1}PbI_3$ perovskite film. To form the control films, the 3D perovskite was subjected to spin-coating at 3000 rpm for 30 seconds with various concentrations of PEAI solution (dissolved in IPA) after cooling. Then, those films were annealed on a hot plate at 100 °C for 10 min. As for LSS films, the prepared 3D perovskite films were first subjected to spin-coating at 3000 rpm for 30 seconds with different concentrations of PCBM in CB solution to form an interlayer, then processed the same way as control films. These films were used for SEM observations. SEM was conducted to examine the 3D surface conditions after treatment with IPA or CB (**Supplementary Fig. 37**). As shown in **Supplementary Fig. 37a-d**, the surface morphology and features exhibit minimal differences between the IPA- and CB-treated 3D samples. Additionally, the XRD results (**Supplementary Fig. 37e**) show no great changes, indicating that the IPA or CB treatment has no obvious effect on the surface condition. A spin-coated spiro-OMeTAD layer and a thermally evaporated gold layer were sequentially deposited on the perovskite films before the fabrication of the STEM specimen.

STEM specimen fabrication and characterization. The cross-sectional TEM specimens of control and LSS PSCs were prepared through a dual-beam focused ion beam (FIB) nanofabrication platform (Helios 5CX, Thermofisher, USA). A 0.3 μm thick platinum (Pt) protection layer was first deposited on the top of the device's metal electrode surface by electron-beam deposition. Then, a 3 μm thick Pt protection layer was deposited by an ion beam to protect the sample area further. The operation voltage of the gallium ion beam was 30 kV, and the working current ranged from 0.1 to 47 nA for lamella processing. Subsequently, the lamella was extracted from the substrate and directly transported to a TEM half-grid in the FIB chamber. The observation area of the lamella was thinned to less than 100 nm using a gallium ion beam with a current ranging from 40 to 790 pA, followed by precise milling and polishing using an ion beam with an accelerating voltage as low as 1 kV and a working current of 72 pA. Carbon layers with a thickness of 10 nm were deposited on both sides of the FIB-ed cross-section specimens for further protection by a high-vacuum coater (Leica ACE 600) at a pressure of 1×10^{-4} mbar. The device cross-section specimens were observed using an aberration-corrected S/TEM (Spectra-300, Thermofisher, USA; equipped with a field emission gun) operating at an accelerating voltage of 300 kV. The probe convergence angle is 24.5 mrad, whereas the angular range of the HAADF detector extended from 79.5 to 200 mrad. The duration that each pixel was exposed during the acquisition of HAADF-STEM images was 6 μs, and the dimensions of all STEM images in this study were 2048 × 2048 pixels. The frame size for the high-resolution STEM images was around 200 × 200 nm^2. The EELS datasets were acquired with an electron beam current of 25 pA using Gatan's K3 single-electron counting direct detection camera. Dual-EELS mode with a dispersion of 0.18 eV/ch, covering the 622 eV energy range, was used to capture the N K-edge, I M-edge, and Br L-edge signals. To obtain a better signal-to-noise ratio (SNR), the I and Br signals were detected separately with different acquisition energy ranges (for I M-edge, 380 eV to 1002 eV; for Br L-edge, 1200 eV to 1822 eV) at the same location. For the 4D STEM measurements, an electron probe with a convergence angle of 1 mrad was used, and the beam current was reduced to below 1 pA (~0.2 pA), thus reducing the electron dose below the threshold values for radiation damage. The 4D STEM datasets were acquired by a pixelated e-detector (EMPAD) with a single exposure of 1 ms and a size of 512 × 512 pixels. Therefore, the cumulative electron dose for a 300 nm × 300 nm acquisition region was approximately 36 $e \cdot Å^{-2}$, which is lower than the 50 $e \cdot Å^{-2}$ critical electron dose that has been documented as causing beam damage in organic and inorganic hybrid perovskite samples.[40-42]

Other material characterizations. SEM images were taken using a Helios 5CX with 3 kV, 86 pA e-beam. The absorption was characterized by the ultraviolet-visible (UV-vis) spectrophotometer (Perkin-Elmer Lambda 35 UV-vis-NIR). Glancing-incident X-ray diffraction (XRD) was performed on a PANAlytical X'pert PRO at an incident angle of XX. Ultraviolet photoelectron spectroscopy (UPS) was characterized by a VG Scienta R4000 analyzer and the HeI (21.22eV) emission line employed for excitation at a bias of -5V. The steady-state photoluminescence spectra were obtained using a pulse laser as an optical excitation source (wavelength: 470 nm, Horiba FluorologFL-

3), and a time-resolved photoluminescence (TRPL) experiment was carried out by excitation at 470 nm. Mott-Schottky was measured by a CHI660E at a frequency of 1 kHz with an applied bias voltage of 0 V~1.4 V. The fluorescence confocal images were obtained by the laser scanning fluorescence confocal microscope (Leica TCS SP8) with 488 nm laser excitation.

Fabrication and testing of inverted PSCs. The MeO-2PACz layer (1 mg/mL in IPA) was deposited on the ITO glass at 3000 rpm for 30 s in a nitrogen-filled glove box, then annealed at 100 ℃ for 10 min. For the preparation of $Cs_{0.05}(MA_{0.05}FA_{0.95})_{0.95}Pb(I_{0.95}Br_{0.05})_3$ perovskite layers, a 1.5 M precursor solution was prepared by dissolving PbI_2 (676.8 mg), FAI (232.8 mg), CsI (19.5 mg), $PbBr_2$ (41.3 mg), and MACl (35.2 mg) in 1 mL of a DMF/DMSO solvent mixture (4:1 volume ratio). The mixture was stirred overnight at room temperature and filtered through a 0.22 μm syringe filter before use. The resultant perovskite precursor solution was then spin-coated at 4000 rpm for 40 s, using 200 μl of EA as the antisolvent at the 30th second. The film was annealed at 120 ℃ for 20 min. For the control device, the PEAI solution (PEAI with different concentrations in IPA) was spin-coated at 3000 rpm for 30 s and annealed at 100 °C for 10 min. For the LSS device, 3D perovskite films were first subjected to spin-coating at 3000 rpm for 30 seconds with different concentrations of PCBM in CB solution to form an interlayer, then be processed the same way as control samples. After forming the control films, the $PC_{61}M$ (20 mg/mL in CB) layer and the BCP (0.7 mg/mL in IPA) film were spin-coated at 2000 rpm and 4000 rpm for the 20s, respectively, then annealed at 70 ℃ for 10 min. Finally, a 100 nm thick layer of Ag was evaporated onto the active area through a mask (0.09 cm^2). Under standard AM 1.5 G illumination using a xenon-lamp-based solar simulator (Enlitech, IVS-KA5000), the current-voltage (*J-V*) characteristic and steady-state power output of solar cells were measured by a Keithley 2420 sourcemeter in the nitrogen-filled glovebox. The light intensity was calibrated by a silicon (Si) diode (Hamamatsu S1133) equipped with a Schott visible-color glass filter (KG5 color filter). The step voltage and scan speeds were 20 mV and 0.2 V s^{-1}. The reference cell for further calibrating the solar simulator before *J-V* measurements was an Oriel® reference solar cell accredited by NIST to the ISO-17025 standard. The area of the metal aperture used during the test is 0.069 cm^2. . EQE was recorded at a chopping frequency of 165 Hz in AC mode on a solar cell quantum efficiency measurement system (QE-R3011, Enlitech). The *p-i-n* PSCs with the configuration of ITO/MeO-2PACz/perovskite/C60/BCP/Ag were fabricated for all stability tests. For the light-soaking stability, the unencapsulated PSCs were tested periodically on continuous one-sun illumination in a nitrogen atmosphere. For the damp heat test, the PSCs were all encapsulated using UV-curing adhesive with a cover glass. Then, the edge of the cover glass was further protected by epoxy and cured at room temperature for >48 hours. The encapsulated devices were placed in an environmental chamber at 85 °C and 85% RH, and the PCEs were measured periodically after the devices cooled to room temperature. Experiments were conducted to determine the unencapsulated devices' long-term operational stability in a flowing nitrogen

atmosphere upon MPP tracking and continuous light irradiation with a white LED lamp (100 mW cm^{-2}).

Data availability

The authors declare that data supporting the findings of this study are available within the paper and its Supplementary Information files. Source data are published with this paper.

Acknowledgments

Y.Z. acknowledges the Excellent Young Scientists Fund (No. 52222318) from the National Natural Science Foundation of China (NSFC), the General Research Fund (Nos. 12302822, 12300923) & the Collaborative Research Fund (No. C2001-23Y) from the Hong Kong Research Grants Council (RGC), the NSFC/RGC Collaborative Research Scheme (No. CRS_HKUST203/23), and the startup grant from the HKUST. Y.Z. also acknowledges the support from the China Merchants Group, particularly China Merchants Testing Certification International Co., Ltd. and China Merchants Research Institute of Advanced Technology Co., Ltd., for translating fundamental research to future technology innovation. S.C. acknowledges the startup grant from the Department of Applied Physics, the Hong Kong Polytechnic University (1-BDCM), the General Research Fund (No. 15306122) & the Early Career Scheme (No. 25305023) from the RGC.

Author contributions

Y. Zhou and S. Cai supervised the project. Z.L., S.C., and Y. Zhou conceived the idea and designed the experiments. Z.L. performed the SEM, STEM, ELLS, and 4D-STEM characterization. W.W. conducted the data analysis of 4D-STEM. P.G. performed the device works, some materials characterizations (PL, XRD, etc.), and stability tests. Y. Zhang contributed to the illustration and assisted in materials characterization. Y. Zhou, S. Cai, Z.L., and P.G. prepared the manuscript. All co-authors contributed to reviewing and revising the manuscript.

Competing interests

The authors declare no competing interests.

Figure Legends/Captions

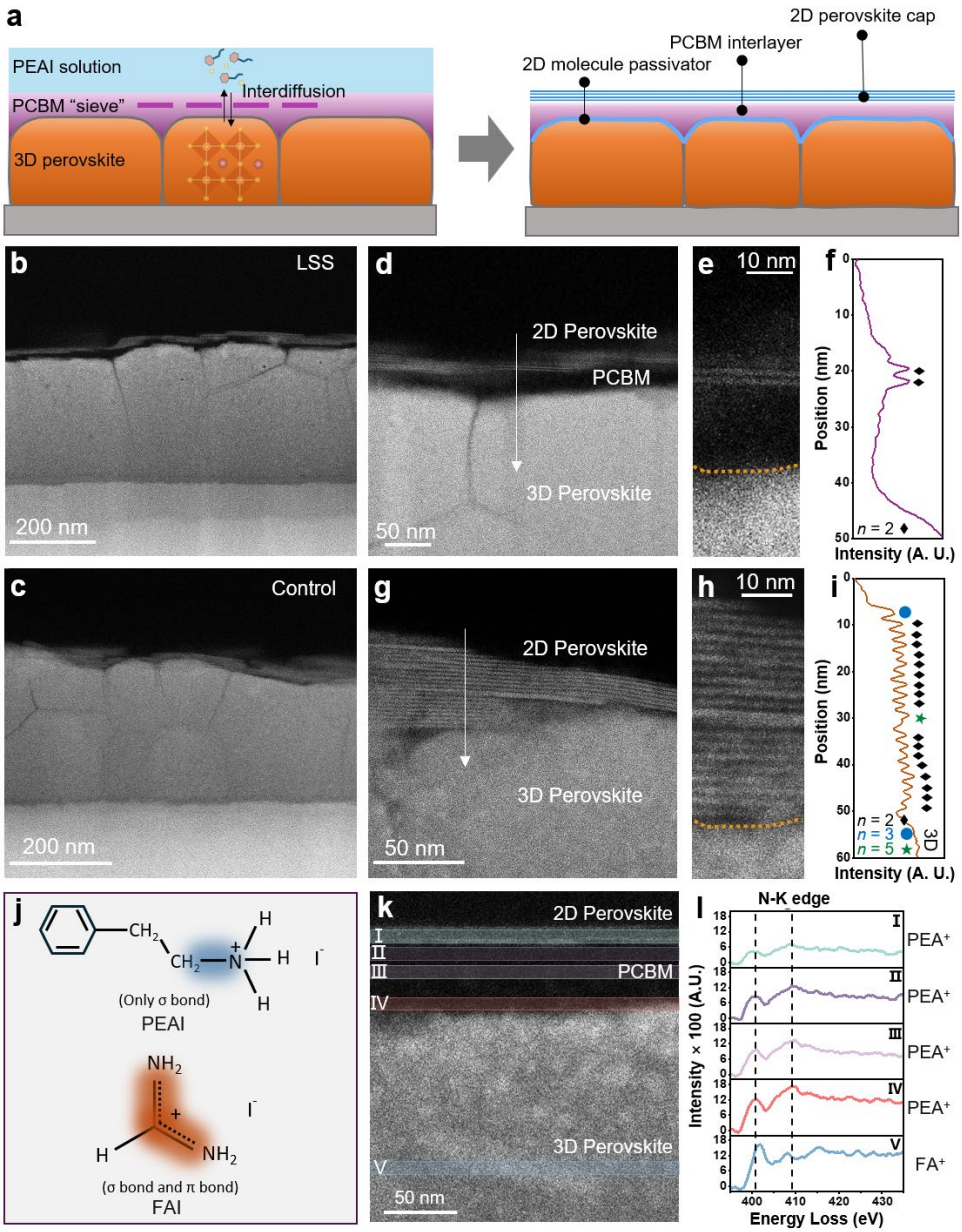

Fig. 1. Lattice-resolved microstructure of perovskite heterointerfaces. a, Schematic illustration of 2D perovskite growth and distribution of LSS sample. **b, d, e,** Cross-sectional HAADF-STEM images of the LSS sample. **f,** Signal intensity line profile of the row marked in (**d**). **c, g, h,** Cross-sectional HAADF-STEM images of the control sample. **i,** Signal intensity line profile of the row marked in (**g**). Layer spacing of $n = 2$, $n = 3$, and n = 5 are 2.20 nm, 2.94 nm, and 4.18 nm, respectively. **j,** PEA^+ only contains C-N σ bond, while FA^+ contains both C-N σ bond and π bond. **k,** N K-edge was signal extracted from regions I-V of the LSS structure. **l,** Non-normalized N K-edge profiles of regions I-V in **k**, demonstrating evident σ bond dominant (PEA^+) characteristics in regions I-IV and π bond characteristics (FA^+) in region V. The N K-edge signal intensity in Region IV is higher than in Region I-III. Region I-V successively refers to the 2D perovskite layer, the top region of the PCBM interlayer, the middle region of the PCBM interlayer, the PCBM/3D perovskite interfacial region, and the 3D perovskite film bulk region.

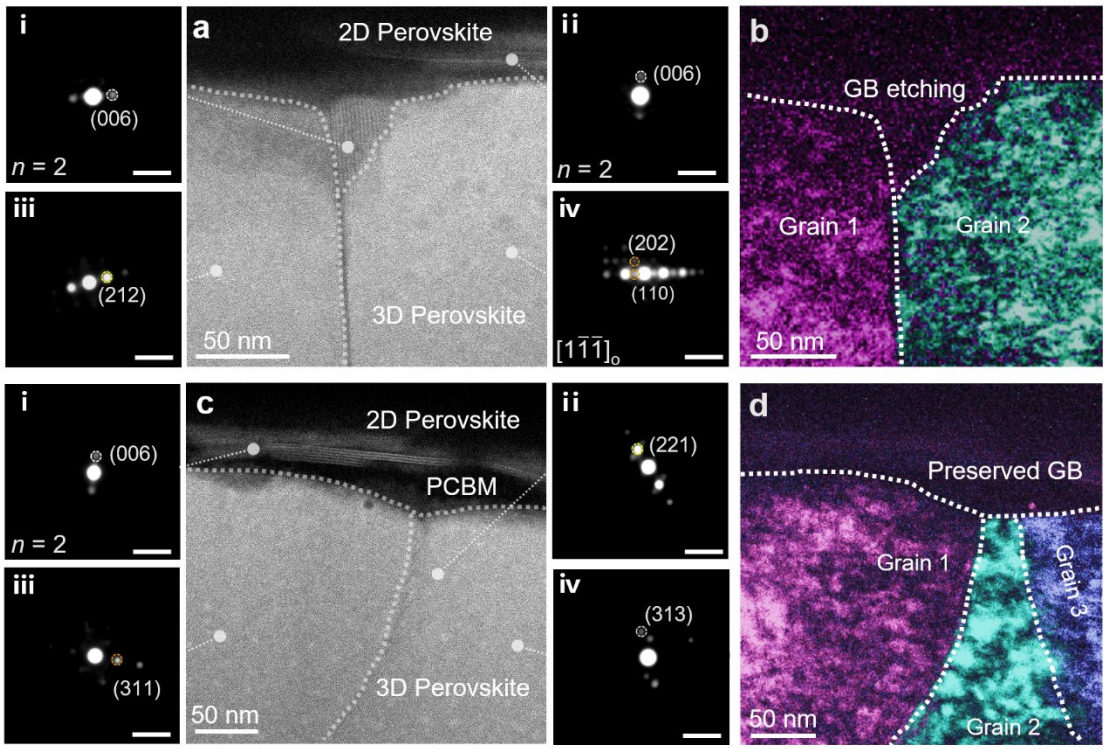

Fig. 2. Near-surface grain-boundary microstructures. a, Cross-sectional HAADF-STEM image of the control sample. The NBED images of the corresponding regions on the control sample. The scale bar is 5 nm^{-1}. **b,** Virtual BF-TEM image reconstructed from NBED signals of regions iii and iv in **a**. **c,** Cross-sectional HAADF-STEM image of the LSS sample. The NBED images of the corresponding region on the LSS sample. The scale bar is 5 nm^{-1}. **d,** Virtual BF-TEM image reconstructed from NBED signals of regions ii-iv in **c**.

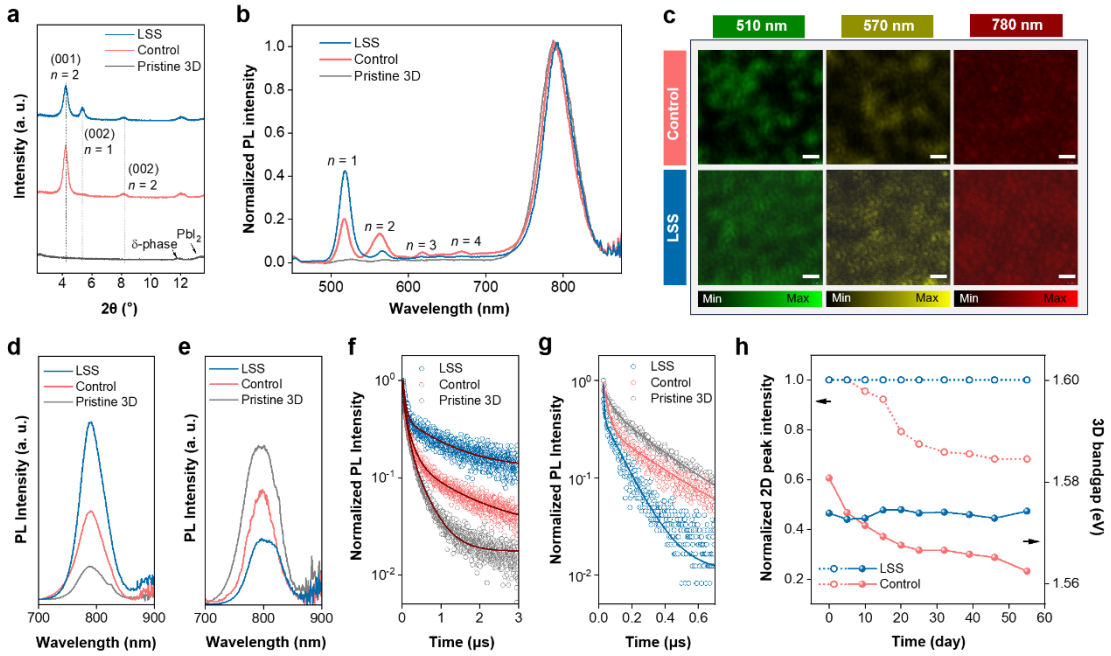

Fig. 3. Optoelectronic properties and stability of perovskite films. a, GIWAX patterns of pristine 3D, control, and LSS films. **b,** Normalized PL spectra of pristine 3D, control, and LSS films. **c,** PL images of control and LSS films at wavelength ~510 nm, 570 nm, and ~780 nm correspond to n = 1 and 2 layers and 3D layers, respectively. The scale bar is 1 μm. Steady-steady PL spectra of pristine 3D, control, and LSS films deposited on bare glass with excitation from glass (**d**) and perovskite (**e**) sides. Time-resolved PL spectra of pristine 3D, control, and LSS films deposited on bare glass with excitation from glass (**f**) and perovskite (**g**) sides. **h,** Evolution of 2D peak and 3D bandgap of control and LSS films by tracking UV-vis spectra under RH of 40%. (LSS: 3D perovskite sample with the PCBM-mediated 2D surface passivation treatment; Control: 3D perovskite sample with conventional 2D surface passivation treatment; Pristine 3D: 3D perovskite sample with no 2D surface passivation treatment.)

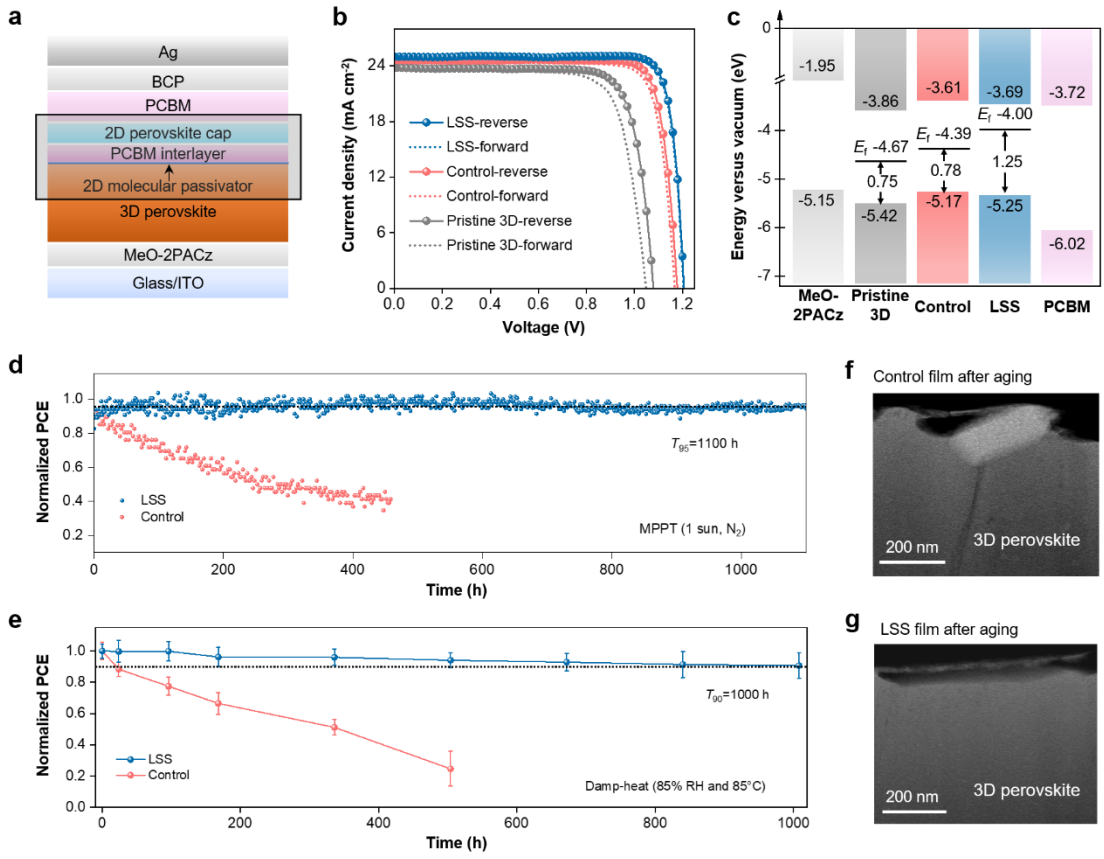

Fig. 4. Photovoltaic performance and long-term stabilities of PSCs. a, Schematic illustration of the device configuration for LSS-based inverted PSCs. **b,** *J-V* curves of the best-performing pristine-3D, control, and LSS PSCs (at both reverse and forward scans). **c,** Energy level scheme for pristine-3D, control, and LSS PSCs extracted from UPS data ([2-(3,6-Dimethoxy-9H-carbazol-9-yl)ethyl]phosphonic acid, MeO-2PACz; bathocuproine, BCP). **d,** Operational stability measured at maximum-power-point tracking in N_2 under continuous one-sun illumination for control and LSS PSCs. The initial PCEs of devices with and without LSS in (**d**) were typically 21.69% and 23.72%, respectively. **e,** Evolution of PCEs of control and LSS PSCs under 85% RH and 85°C (sample size n = 13 for both cases). Error bars in (**e**) represent the standard deviation of the measurements obtained from five samples in both cases. **f, g,** HAADF-STEM images of control and LSS films after the identical damp-heat aging. (LSS: 3D perovskite sample with the PCBM-mediated 2D surface passivation treatment; Control: 3D perovskite sample with conventional 2D surface passivation treatment; Pristine 3D: 3D perovskite sample with no 2D surface passivation treatment.)

References

1 Chen, S., Deng, Y., Gu, H., Xu, S., Wang, S., Yu, Z., Blum, V. & Huang, J. Trapping lead in perovskite solar modules with abundant and low-cost cation-exchange resins. *Nature Energy* **5**, 1003-1011 (2020).

2 Yoo, J. J., Seo, G., Chua, M. R., Park, T. G., Lu, Y., Rotermund, F., Kim, Y.-K., Moon, C.

S., Jeon, N. J., Correa-Baena, J.-P., Bulović, V., Shin, S. S., Bawendi, M. G. & Seo, J. Efficient perovskite solar cells via improved carrier management. *Nature* **590**, 587-593 (2021).

3 Čulík, P., Brooks, K., Momblona, C., Adams, M., Kinge, S., Maréchal, F., Dyson, P. J. & Nazeeruddin, M. K. Design and Cost Analysis of 100 MW Perovskite Solar Panel Manufacturing Process in Different Locations. *ACS Energy Letters* **7**, 3039-3044 (2022).

4 Liu, X., Zheng, B., Shi, L., Zhou, S., Xu, J., Liu, Z., Yun, J. S., Choi, E., Zhang, M. & Lv, Y. J. N. P. Perovskite solar cells based on spiro-OMeTAD stabilized with an alkylthiol additive. *Nature Photonics* **17**, 96-105 (2023).

5 Zhang, T., Wang, F., Kim, H.-B., Choi, I.-W., Wang, C., Cho, E., Konefal, R., Puttisong, Y., Terado, K. & Kobera, L. J. S. Ion-modulated radical doping of spiro-OMeTAD for more efficient and stable perovskite solar cells. *Science* **377**, 495-501 (2022).

6 Tan, Q., Li, Z., Luo, G., Zhang, X., Che, B., Chen, G., Gao, H., He, D., Ma, G., Wang, J., Xiu, J., Yi, H., Chen, T. & He, Z. Inverted perovskite solar cells using dimethylacridine-based dopants. *Science* **620**, 545-551 (2023).

7 Chen, H., Liu, C., Xu, J., Maxwell, A., Zhou, W., Yang, Y., Zhou, Q., Bati, A. S., Wan, H. & Wang, Z. J. S. Improved charge extraction in inverted perovskite solar cells with dual-site-binding ligands. *Science* **384**, 189-193 (2024).

8 Ye, F., Zhang, S., Warby, J., Wu, J., Gutierrez-Partida, E., Lang, F., Shah, S., Saglamkaya, E., Sun, B. & Zu, F. J. N. C. Overcoming C60-induced interfacial recombination in inverted perovskite solar cells by electron-transporting carborane. *Nature Communications* **13**, 7454 (2022).

9 Chen, J., Luo, J., Hou, E., Song, P., Li, Y., Sun, C., Feng, W., Cheng, S., Zhang, H. & Xie, L. J. N. P. Efficient tin-based perovskite solar cells with trans-isomeric fulleropyrrolidine additives. *Nature Photonics*, 1-7 (2024).

10 Li, Z., Sun, X., Zheng, X., Li, B., Gao, D., Zhang, S., Wu, X., Li, S., Gong, J., Luther, J. M., Li, Z. a. & Zhu, Z. Stabilized hole-selective layer for high-performance inverted p-i-n perovskite solar cells. *Science* **382**, 284-289 (2023).

11 Azmi, R., Utomo, D. S., Vishal, B., Zhumagali, S., Dally, P., Risqi, A. M., Prasetio, A., Ugur, E., Cao, F., Imran, I. F., Said, A. A., Pininti, A. R., Subbiah, A. S., Aydin, E., Xiao, C., Seok, S. I. & De Wolf, S. Double-side 2D/3D heterojunctions for inverted perovskite solar cells. *Nature* **628**, 93-98 (2024).

12 Azmi, R., Ugur, E., Seitkhan, A., Aljamaan, F., Subbiah, A. S., Liu, J., Harrison, G. T., Nugraha, M. I., Eswaran, M. K., Babics, M., Chen, Y., Xu, F., Allen, T. G., Rehman, A. u., Wang, C.-L., Anthopoulos, T. D., Schwingenschlögl, U., De Bastiani, M., Aydin, E. & De Wolf, S. Damp heat–stable perovskite solar cells with tailored-dimensionality 2D/3D heterojunctions. *Science* **376**, 73-77 (2022).

13 Jang, Y.-W., Lee, S., Yeom, K. M., Jeong, K., Choi, K., Choi, M. & Noh, J. H. Intact 2D/3D halide junction perovskite solar cells via solid-phase in-plane growth. *Nature Energy* **6**, 63-71 (2021).

14 Sidhik, S., Wang, Y., De Siena, M., Asadpour, R., Torma, A. J., Terlier, T., Ho, K., Li, W., Puthirath, A. B., Shuai, X., Agrawal, A., Traore, B., Jones, M., Giridharagopal, R., Ajayan, P. M., Strzalka, J., Ginger, D. S., Katan, C., Alam, M. A., Even, J., Kanatzidis, M. G. & Mohite, A. D. Deterministic fabrication of 3D/2D perovskite bilayer stacks for durable and

efficient solar cells. *Science* **377**, 1425-1430 (2022).
15 Zhong, Y., Liu, G., Su, Y., Sheng, W., Gong, L., Zhang, J., Tan, L. & Chen, Y. Diammonium Molecular Configuration-Induced Regulation of Crystal Orientation and Carrier Dynamics for Highly Efficient and Stable 2D/3D Perovskite Solar Cells. *Angewandte Chemie International Edition* **61** (2021).
16 Yang, T., Ma, C., Cai, W., Wang, S., Wu, Y., Feng, J., Wu, N., Li, H., Huang, W., Ding, Z., Gao, L., Liu, S. & Zhao, K. Amidino-based Dion-Jacobson 2D perovskite for efficient and stable 2D/3D heterostructure perovskite solar cells. *Joule* **7**, 574-586 (2023).
17 Chen, H., Teale, S., Chen, B., Hou, Y., Grater, L., Zhu, T., Bertens, K., Park, S. M., Atapattu, H. R., Gao, Y., Wei, M., Johnston, A. K., Zhou, Q., Xu, K., Yu, D., Han, C., Cui, T., Jung, E. H., Zhou, C., Zhou, W., Proppe, A. H., Hoogland, S., Laquai, F., Filleter, T., Graham, K. R., Ning, Z. & Sargent, E. H. Quantum-size-tuned heterostructures enable efficient and stable inverted perovskite solar cells. *Nature Photonics* **16**, 352-358 (2022).
18 Luo, L., Zeng, H., Wang, Z., Li, M., You, S., Chen, B., Maxwell, A., An, Q., Cui, L. & Luo, D. J. N. E. Stabilization of 3D/2D perovskite heterostructures via inhibition of ion diffusion by cross-linked polymers for solar cells with improved performance. *Nature Energy* **8**, 294-303 (2023).
19 Li, B., Liu, Q., Gong, J., Li, S., Zhang, C., Gao, D., Chen, Z., Li, Z., Wu, X. & Zhao, D. J. N. C. Harnessing strong aromatic conjugation in low-dimensional perovskite heterojunctions for high-performance photovoltaic devices. *Nature Communications* **15**, 2753 (2024).
20 Cai, S., Dai, J., Shao, Z., Rothmann, M. U., Jia, Y., Gao, C., Hao, M., Pang, S., Wang, P., Lau, S. P., Zhu, K., Berry, J. J., Herz, L. M., Zeng, X. C. & Zhou, Y. Atomically Resolved Electrically Active Intragrain Interfaces in Perovskite Semiconductors. *Journal of the American Chemical Society* **144**, 1910-1920 (2022).
21 Cai, S., Li, Z., Zhang, Y., Liu, T., Wang, P., Ju, M.-G., Pang, S., Lau, S. P., Zeng, X. C. & Zhou, Y. Intragrain impurity annihilation for highly efficient and stable perovskite solar cells. *Nature Communications* **15**, 2329 (2024).
22 deQuilettes, D. W., Yoo, J. J., Brenes, R., Kosasih, F. U., Laitz, M., Dou, B. D., Graham, D. J., Ho, K., Shi, Y., Shin, S. S., Ducati, C., Bawendi, M. G. & Bulović, V. Reduced recombination via tunable surface fields in perovskite thin films. *Nature Energy* **9**, 457-466 (2024).
23 Li, H., Zhang, C., Gong, C., Zhang, D., Zhang, H., Zhuang, Q., Yu, X., Gong, S., Chen, X., Yang, J., Li, X., Li, R., Li, J., Zhou, J., Yang, H., Lin, Q., Chu, J., Grätzel, M., Chen, J. & Zang, Z. 2D/3D heterojunction engineering at the buried interface towards high-performance inverted methylammonium-free perovskite solar cells. *Nature Energy* **8**, 946-955 (2023).
24 Zhou, Y., Herz, L. M., Jen, A. K. & Saliba, M. J. N. E. Advances and challenges in understanding the microscopic structure–property–performance relationship in perovskite solar cells. *Nature Energy* **7**, 794-807 (2022).
25 Chen, J., Quan, X., Lu, M., Niu, Y. & Zhang, B. J. U. Quantitative Analysis Method for Nitrogen Electron Energy-Loss Near-Edge Structures in Nanocarbons Based on Density Functional Theory Calculations and Linear Regression. *Ultramicroscopy* **215**, 113006 (2020).

26 Yan, L., Huang, H., Cui, P., Du, S., Lan, Z., Yang, Y., Qu, S., Wang, X., Zhang, Q., Liu, B., Yue, X., Zhao, X., Li, Y., Li, H., Ji, J. & Li, M. Fabrication of perovskite solar cells in ambient air by blocking perovskite hydration with guanabenz acetate salt. *Nature Energy* **8**, 1158-1167 (2023).
27 Hao, M., Duan, T., Ma, Z., Ju, M. G., Bennett, J. A., Liu, T., Guo, P. & Zhou, Y. Flattening Grain-Boundary Grooves for Perovskite Solar Cells with High Optomechanical Reliability. *Advanced Materials* **35**, 2211155 (2023).
28 Suo, J., Yang, B., Mosconi, E., Bogachuk, D., Doherty, T. A. S., Frohna, K., Kubicki, D. J., Fu, F., Kim, Y., Er-Raji, O., Zhang, T., Baldinelli, L., Wagner, L., Tiwari, A. N., Gao, F., Hinsch, A., Stranks, S. D., De Angelis, F. & Hagfeldt, A. Multifunctional sulfonium-based treatment for perovskite solar cells with less than 1% efficiency loss over 4,500-h operational stability tests. *Nature Energy* **9**, 172-183 (2024).
29 Ghasemi, M., Guo, B., Darabi, K., Wang, T., Wang, K., Huang, C.-W., Lefler, B. M., Taussig, L., Chauhan, M., Baucom, G., Kim, T., Gomez, E. D., Atkin, J. M., Priya, S. & Amassian, A. A multiscale ion diffusion framework sheds light on the diffusion–stability–hysteresis nexus in metal halide perovskites. *Nature Materials* **22**, 329-337 (2023).
30 You, S., Zeng, H., Liu, Y., Han, B., Li, M., Li, L., Zheng, X., Guo, R., Luo, L. & Li, Z. J. S. Radical polymeric p-doping and grain modulation for stable, efficient perovskite solar modules. *Science* **379**, 288-294 (2023).
31 Xiao, T., Hao, M., Duan, T., Li, Y., Zhang, Y., Guo, P. & Zhou, Y. J. N. E. Elimination of grain surface concavities for improved perovskite thin-film interfaces. *Nature Energy* **9**, 999-1010 (2024).
32 Mu, X., Mazilkin, A., Sprau, C., Colsmann, A. & Kübel, C. J. M. Mapping structure and morphology of amorphous organic thin films by 4D-STEM pair distribution function analysis. *Microscopy* **68**, 301-309 (2019).
33 Roccapriore, K. M., Dyck, O., Oxley, M. P., Ziatdinov, M. & Kalinin, S. V. J. A. n. Automated experiment in 4D-STEM: exploring emergent physics and structural behaviors. *ACS nano* **16**, 7605-7614 (2022).
34 Doherty, T. A., Nagane, S., Kubicki, D. J., Jung, Y.-K., Johnstone, D. N., Iqbal, A. N., Guo, D., Frohna, K., Danaie, M. & Tennyson, E. M. J. S. Stabilized tilted-octahedra halide perovskites inhibit local formation of performance-limiting phases. *Science* **374**, 1598-1605 (2021).
35 Macpherson, S., Doherty, T. A. S., Winchester, A. J., Kosar, S., Johnstone, D. N., Chiang, Y.-H., Galkowski, K., Anaya, M., Frohna, K., Iqbal, A. N., Nagane, S., Roose, B., Andaji-Garmaroudi, Z., Orr, K. W. P., Parker, J. E., Midgley, P. A., Dani, K. M. & Stranks, S. D. Local nanoscale phase impurities are degradation sites in halide perovskites. *Nature* **607**, 294-300 (2022).
36 Ophus, C. Four-Dimensional Scanning Transmission Electron Microscopy (4D-STEM): From Scanning Nanodiffraction to Ptychography and Beyond. *Microscopy and Microanalysis* **25**, 563-582 (2019).
37 Wang, D., Wang, P., Mondal, S., Hu, M., Wang, D., Wu, Y., Ma, T. & Mi, Z. Thickness scaling down to 5 nm of ferroelectric ScAlN on CMOS compatible molybdenum grown by molecular beam epitaxy. *Applied Physics Letters* **122** (2023).
38 Almora, O., Cabrera, C. I., Garcia-Cerrillo, J., Kirchartz, T., Rau, U. & Brabec, C. J. J. A.

e. m. Quantifying the absorption onset in the quantum efficiency of emerging photovoltaic devices. *Advanced Energy Materials* **11**, 2100022 (2021).

39 Jeong, M., Choi, I. W., Go, E. M., Cho, Y., Kim, M., Lee, B., Jeong, S., Jo, Y., Choi, H. W. & Lee, J. J. S. Stable perovskite solar cells with efficiency exceeding 24.8% and 0.3-V voltage loss. *Science* **369**, 1615-1620 (2020).

40 Rothmann, M. U., Kim, J. S., Borchert, J., Lohmann, K. B., O'Leary, C. M., Sheader, A. A., Clark, L., Snaith, H. J., Johnston, M. B. & Nellist, P. D. J. S. Atomic-scale microstructure of metal halide perovskite. *Science* **370**, eabb5940 (2020).

41 Yang, C. Q., Zhi, R., Rothmann, M. U., Xu, Y. Y., Li, L. Q., Hu, Z. Y., Pang, S., Cheng, Y. B., Van Tendeloo, G. & Li, W. J. A. M. Unveiling the intrinsic structure and intragrain defects of organic–inorganic hybrid perovskites by ultralow dose transmission electron microscopy. *Advanced Materials* **35**, 2211207 (2023).

42 Chen, S., Wu, C., Han, B., Liu, Z., Mi, Z., Hao, W., Zhao, J., Wang, X., Zhang, Q. & Liu, K. J. N. C. Atomic-scale imaging of $CH_3NH_3PbI_3$ structure and its decomposition pathway. *Nature Communications* **12**, 5516 (2021).